



Autogenous Tungsten Inert Gas Welding of 430 Ferritic Stainless Steel: The Effect of Inter-pass Temperature on Microstructure Evolution and Mechanical Properties

Mohammad Ali Mousazadeh and Reza Derakhshandeh-Haghighi

Submitted: 10 April 2020 / Revised: 18 October 2020 / Accepted: 25 October 2020 / Published online: 9 November 2020

Effect of inter-pass temperature on the microstructure evolution and mechanical properties of AISI 430 ferritic stainless steel welded by autogenous tungsten inert gas (TIG) technique was investigated. The relationship between the structure and the property of the weldments with inter-pass temperature and without inter-pass temperature is elaborated in this study. Microstructure studies depicted the presence of martensite in the weld metal and some parts of the heat affected zone (HAZ). Increasing inter-pass temperature resulted in higher amount of martensite both in the weld metal and in the HAZ. In addition, high inter-pass temperatures resulted in large HAZ width and grain growth which in turn led to poor tensile strength and ductility of the weldments. An optimum inter-pass temperature of 150 °C provided the best mechanical properties. However, it was inferred that when it is not possible to have a precise control on inter-pass temperature during manufacturing AISI 430 joints, it is better to complete welding without applying inter-pass temperature in order to at least keep tensile strength and ductility of the weldments.

Keywords 430 ferritic stainless steel, cooling rate, inter-pass temperature, microstructural characterization, TIG welding

1. Introduction

Ferritic stainless steels (FSS) are good substitute for austenitic stainless steels. FSS in the absence of nickel provides moderate corrosion resistance at lower cost (Ref 1). FSS has good toughness, ductility, weldability and excellent resistance to stress corrosion cracking, in comparison with austenitic stainless steels (Ref 2). Ferritic stainless steels are used to a greater extent in automotive exhaust components and combustion chambers due to their excellent resistance to chloride-induced stress corrosion cracking, adequate high-temperature strength, good resistance to oxidation and wet corrosion and sufficient resistance to thermal fatigue (Ref 3, 4). FSS shows lower coefficient of expansion in comparison with austenitic stainless steel, which is important when resistance to cyclic temperature is needed (Ref 5, 6). As a major route, welding is adopted for fabrication of different components made by these alloys. Gas tungsten arc welding (GTAW) is generally used for fabrication of components made by FSS because of a very high-quality weld. However, these alloys suffer from grain coarsening in the weld metal (WM) and heat-affected zone (HAZ) (Ref 7). Precipitation of secondary phases and grain growth in high-chromium FSS in HAZ and WM leads to loss of

mechanical properties particularly lower ductility and toughness (Ref 8, 9). By applying low heat input processes such as laser beam welding or solid-state welding, grain growth and precipitation of deleterious phases such as sigma could be controlled (Ref 9, 10). Other challenges include a wide brittle to ductile transition temperature and loss of high-temperature oxidation resistance (Ref 11).

The microstructure of ferritic stainless steels could be either fully ferritic or a mixture of ferrite and martensite. Martensite occupies the grain boundaries. The austenite solid-state transformation is the common path in 430 FSS for the formation of grain boundary martensite (Ref 8). Alizadeh-Sh et al. (Ref 12) investigated the relationship between microstructure and performance in resistance spot welding of 430 ferritic stainless steel. They discussed the mechanical properties of the welds based on different metallurgical transformations in HAZ and WM. Friction stir welding (FSW) was applied on 430 ferritic stainless steel sheets by Bilgin et al. (Ref 9). It was found that the formation of deleterious phases and also excessive grain growth could be overcome. Ramkumar et al. (Ref 13) investigated the weldability of AISI 430 ferritic stainless steel, by tungsten inert gas (TIG) welding technique with and without the use of activated fluxes at different heat inputs. Mallaiah et al. (Ref 10) studied the effect of grain refining elements on mechanical properties of AISI 430 ferritic stainless steel welds through GTAW process. They could achieve high strength and also an improvement in ductility when optimum amount of Cu, Ti and Al was added as grain refining elements. Khan et al. (Ref 14) studied the influence of different welding parameters on the microstructure and hardness in laser beam welding of AISI 304L to AISI 430 stainless steels. It was found that intergranular carbides and continuous martensitic layer along ferrite grain boundaries are formed. Effect of post-weld heat treatment on microstructural and mechanical properties of 430-304 stainless steel joints was investigated by ghorbani et al. (Ref 15). They found that post-weld heat treatment results in

Mohammad Ali Mousazadeh, Department of Materials Science and Engineering, Bandar Abbas Branch, Islamic Azad University, Bandar Abbas, Iran; and **Reza Derakhshandeh-Haghighi**, Department of Materials Science and Engineering, Shiraz Branch, Islamic Azad University, Shiraz, Iran. Contact e-mail: derakhshandeh@shirazu.ac.ir.

dissolution of chromium precipitates and decrease the martensitic grain size.

One of the important factors in welding is controlling inter-pass temperature. Inter-pass temperature determines the cooling rates that will be experienced by the weld metal and the surrounding material. The cooling rate must be properly controlled to ensure that the resultant weld metal will have the required properties. When welding ferrous alloys, a controlled inter-pass temperature slows the cooling rate through an alloy's critical temperature to prevent defects from happening during multipass welding (Ref 16). Ginn et al. (Ref 17) tested some austenitic stainless steels and welding processes with different inter-pass temperatures ranging from 100 to 400 °C. The results show that higher inter-pass temperatures have no effect on mechanical properties and weld microstructure. According to a study of a dissimilar joint between carbon steel and austenitic stainless steel by Omar (Ref 18), an optimum preheat and inter-pass temperature and also electrode composition for the weld joint were recommended. Lee (Ref 19) studied inter-pass temperature in austenitic stainless steel as a welding variable. It was shown that increasing preheat and inter-pass temperature results in increasing the degree of sensitization and the width of the sensitized zone. Sam et al. (Ref 20) examined the formation of delta-ferrite in a ferritic-martensitic stainless steel TIG welded at different preheat temperatures. They found that the volume fraction of delta-ferrite decreases by increasing preheat temperature.

In welds that are fully ferritic, preheat or controlling inter-pass temperature is not necessary and may exacerbate grain growth (Ref 8). However, when duplex ferritic/martensitic structure in AISI 430 stainless steel is encountered after welding, controlling inter-pass temperature seems to have significant influence on the properties of the weld. In fact, the amount of cooling rate should be controlled to reach an optimum amount of martensite and other precipitates in such steels. Although several research works exist on the welding of ferritic stainless steels, the understanding of intricate issues in controlling inter-pass temperature seems to be vital. In the present work, the influence of inter-pass temperature on microstructural and mechanical properties of AISI 430 stainless steel has been studied. The outcomes of the research reported in this article will be beneficial to the industries employing AISI 430 stainless steel.

2. Experimental Procedure

The chemical composition of the as-received base metal which is represented in Table 1, was evaluated by emission spectroscopy analysis. Some physical properties of AISI 430 stainless steel are presented in Table 2.

Before welding, the as-received plate of the base metal was cut to the dimension of 200 × 100 × 3 mm, and a double V-

groove was machined. A double-pass autogenous TIG welding trials were applied for five different inter-pass temperatures. A 2.4 mm 2% thoriated tungsten electrode with a tip angle of 60° was used for welding trials. Table 3 shows the inter-pass temperatures and process parameters employed for autogenous TIG welding to achieve complete penetrating joints. Inter-pass temperatures were measured by using an infrared thermometer before applying the second pass. Both optical microscopy (OM) and scanning electron microscopy (SEM) techniques were used to determine the microstructural changes. Metallographic procedures were applied by grinding using 120 to 2500 grit SiC papers and then disk polishing using alumina and distilled water solution. Etching in Kalling's solution (5 g CuCl₂ + 100 ml HCl + 100 ml Ethanol) was used to reveal the microstructure of the joints. For optical microscopy, a Metallux 3 Leitz microscope equipped with Clemex software was used to determine the surface fraction of second phases on the ferrite grain boundaries. Chemical composition of various locations of the weldments was determined by point EDAX analysis with VEGA/Tescan-LMU SEM. For better understanding of the types of the precipitates in the welds, XRD analysis was conducted. Transverse tensile test was performed on the coupons at room temperature, according to ASTM-E8 standard. Three tensile trials in each case of the weldments were carried out using Instron Universal Testing Machine with a constant cross-head velocity of 5 mm/s. Moreover, the fracture surfaces were characterized by SEM analysis to investigate the mode of fracture in different weldments. Vickers microhardness (HV) measurements were carried out on cross-sectioned coupons at different regions such as base metal, HAZ and weld metal. A standard load of 500 gf for a dwell period of 15 s at regular intervals of 0.25 mm was applied by using a Koopa microhardness tester. In order to obtain statistically reliable results, hardness tests were carried out using three specimens for each individual material testing.

3. Results

3.1 Microstructure Examination in the Base Metal and HAZ

The Fe–Cr–C ternary system is used to describe the phase transformation in AISI 430 stainless steel. Figure 1 illustrates the pseudo-binary diagram at 17 wt.% Cr with a nominal carbon concentration of 0.05 wt.% (Ref 8). One can find out that this composition approximates that of AISI 430 stainless steel. According to this phase diagram, under equilibrium cooling condition the final microstructure will be a mixture of ferrite and carbide. Figure 2(a) shows the optical micrograph of the base metal for AISI 430 stainless steel. This microstructure includes ferrite grains and carbides which are distributed in the rolling direction. Figure 2(b) presents the macrograph of T25 and T750 specimens including weld metal and HAZ.

Table 1 Nominal chemical composition (wt.%) of the base metal used in this study

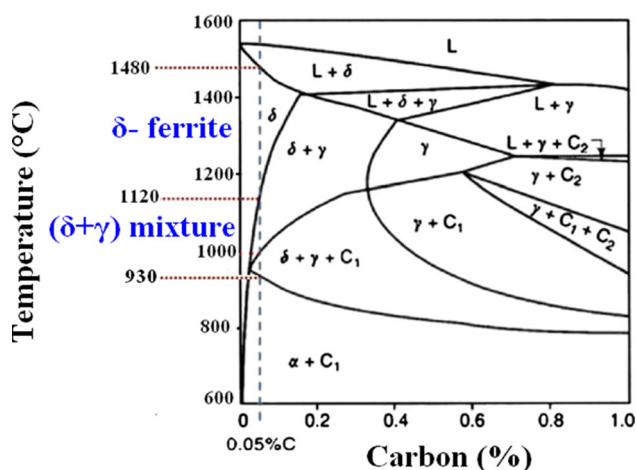
Chemical composition, wt.%									
Alloy	C	Mn	Si	Cr	Ni	Mo	Cu	Sn	Fe
AISI 430	0.05	0.43	0.31	16.6	0.15	0.012	0.025	0.018	Bal.

Table 2 Some physical properties of AISI 430 stainless steel

Alloy AISI 430	Density, g cm ⁻³	Thermal conductivity, W m ⁻¹ K ⁻¹	Specific heat, J Kg ⁻¹ K ⁻¹	Melting point, °C
	7.8	26.3	460	1510

Table 3 The inter-pass temperatures and process parameters employed for autogenous TIG welding

# Specimen	Inter-pass temperature, °C	Welding current, A	Arc voltage, V	Welding speed, mm s ⁻¹	Gas flow rate, l min ⁻¹
T750	750	160	22	4	5
T550	550				
T350	350				
T150	150				
T25	25 (room temp.)				

**Fig. 1** Fe–Cr–C pseudo-binary diagram at 17% Cr (Ref 8)

Based on the phase diagram in Fig. 1, fully δ -ferrite microstructure can be obtained in the region next to fusion zone where heat-affected zone experiences temperatures between approximately 1120–1480 °C. This region is called high-temperature heat-affected zone. Upon fast cooling after welding, the transformation of ferrite to austenite at elevated temperature is suppressed, and therefore, no martensite phase is formed at grain boundaries. It has been also reported by other researchers (Ref 12, 21). The grain growth is pronounced in 430 HAZ near the fusion zone due to high thermal conductivity and absence of phase change that does not allow the grain refinement (Ref 21). In the absence of grain boundary austenite, the ferrite grains grow rapidly and the HAZ exhibits relatively large grains. However, away from the fusion zone the condition for formation of a mixture of ferrite and austenite is provided in which upon cooling austenite transforms to martensite along the ferrite grain boundaries. The growth of ferrite grains will stop once austenite starts to form along grain boundaries. The difference between phase transformation in HAZ near fusion zone and away from it means that they have significantly different properties. Figure 2(c) and (d) shows optical micrographs of the HAZ at the interface of the fully δ -ferrite microstructure near the fusion line (high-temperature heat-affected zone) and the mixture of δ -ferrite and martensite ($\delta + M$) away from the fusion line for T25 and T750

specimens, respectively. Because of the absence of austenite at grain boundaries, ferrite grain growth in high-temperature heat-affected zone is remarkable. High inter-pass temperature results in larger grain size at δ -ferrite region and also thicker martensite plates at grain boundaries. In fact at high inter-pass temperatures (Fig. 2d), cooling rate decreases and austenite will have more time to form at grain boundaries. By further cooling, the grain boundaries which are rich in austenite transform to thick martensite plates.

Figure 3(a), (b), (c), (d), and (e) shows HAZ for the specimens away from the fusion line at 750, 550, 350, 150 and 25 °C inter-pass temperatures, respectively. According to Fig. 1, by moving from the fusion line the temperature decreases and some austenite forms along ferrite grain boundaries.

3.2 Microstructure Examination in the Weld Metal

In order to reach an in-depth conclusion, we need to study the metallurgical phenomena happening in the weld metal. Figure 4(a), (b), (c), (d), and (e) shows the optical micrographs of the weld metals at 750, 550, 350, 150 and 25 °C, inter-pass temperatures, respectively. The martensite as a continuous grain boundary phase is present along the ferrite grain boundaries. According to this micrograph as inter-pass temperature decreases, the amount of martensite on the ferrite grain boundaries decreases. T750 specimen with the highest inter-pass temperature has the highest amount of thick martensitic plates (Fig. 4a), whereas T25 contains the least amount of martensite (Fig. 4e).

Figure 5(a) and (b) illustrates the areas detected as martensite by Clemex software for T25 weld metal and T750 HAZ, respectively. The fraction of area covered by martensite in the weld metal and the HAZ estimated by Clemex software for the samples studied in this research is seen in Fig. 5(c). According to this figure, by decreasing inter-pass temperature the fraction of area covered by martensite decreases both for the weld metal and the HAZ. Moreover, this fraction is lower for the weld metal than the HAZ because of higher cooling rates that the weld metal experiences during cooling to room temperature. In fact, higher cooling rates diminishes the amount of austenite (γ) on ferrite grain boundaries; therefore, less martensite forms from austenite.

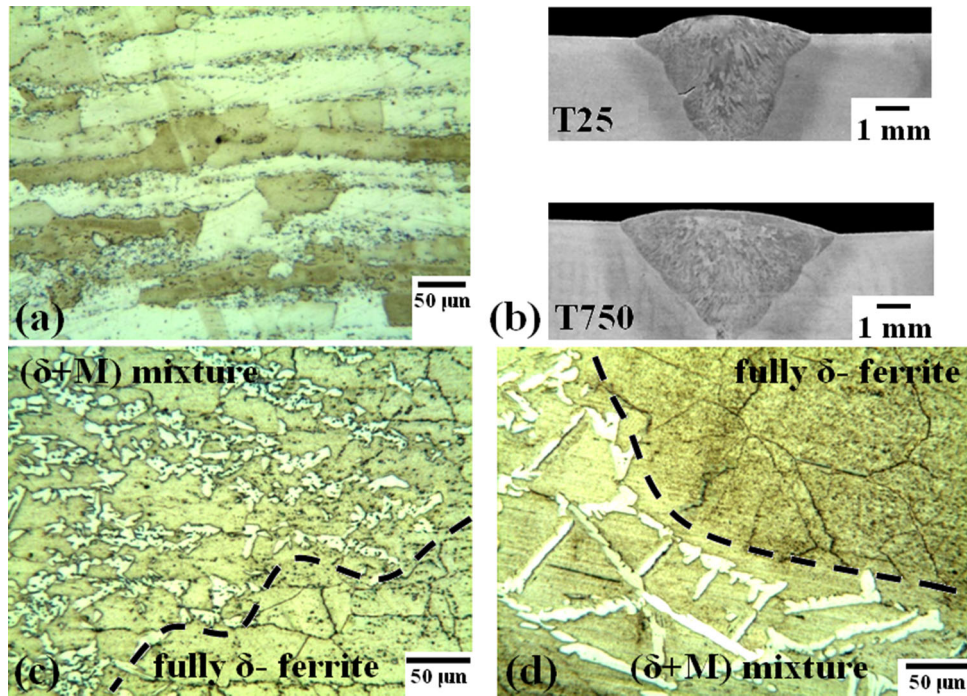


Fig. 2 The optical micrograph of the as-received AISI 430 stainless steel base metal (a) the macrograph of the weld metal for T25 and T750 specimen (b) the optical micrographs of the HAZ at the interface of the fully δ -ferrite region and duplex-phase region of $(\delta + M)$ at different inter-pass temperatures (c) 25 °C (d) 750 °C

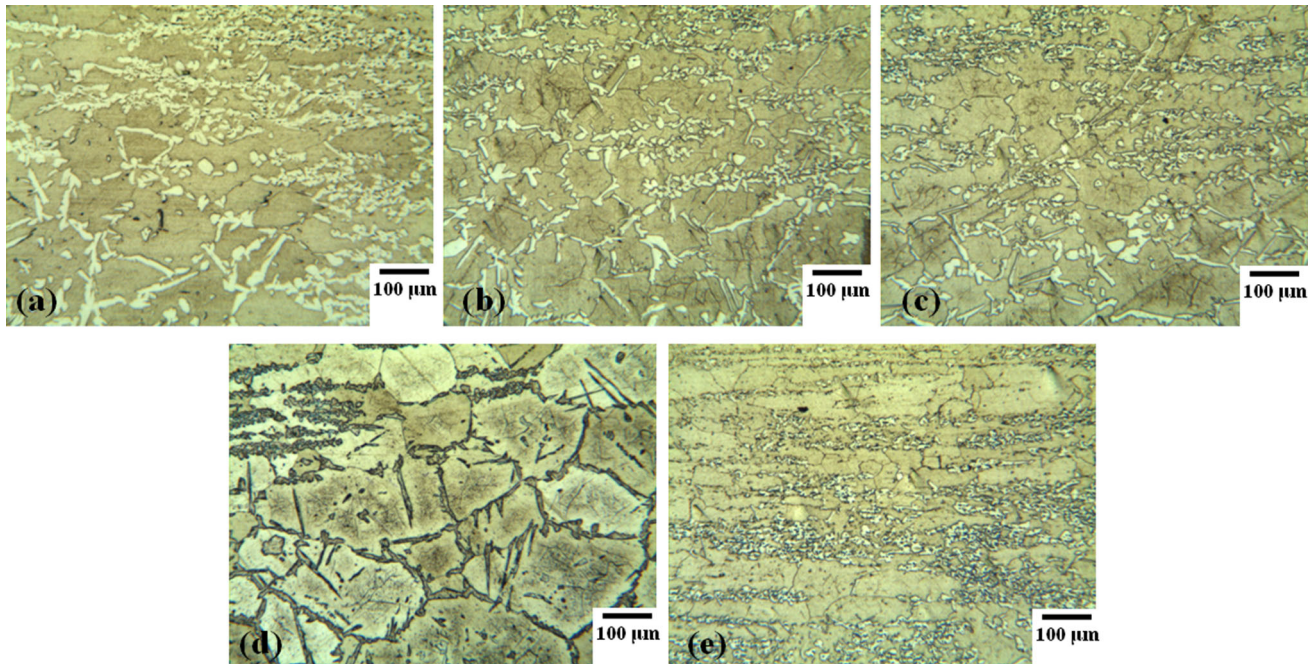


Fig. 3 The optical micrographs of the HAZ away from the fusion line at different inter-pass temperatures (a) 750 °C (b) 550 °C (c) 350 °C (d) 150 °C and (e) 25 °C

Under very slow cooling, the elevated temperature austenite transforms to ferrite and carbides as is predicted by phase diagram in Fig. 1. However, during welding any elevated temperature austenite will transform to martensite upon cooling to room temperature. The Kaltenhauser ferrite factor (Eq 1) is used to predict whether the microstructure contains martensite (Ref 22). In medium-chromium alloys such as type 430

stainless steel, k -factor must exceed 17 to prevent martensite formation in the weld metal.

$$k\text{-factor} = \text{Cr} + 6\text{Si} + 8\text{Ti} + 4\text{Mo} + 2\text{Al} - 40(\text{C} + \text{N}) - 2\text{Mn} - 4\text{Ni} \quad (\text{Eq 1})$$

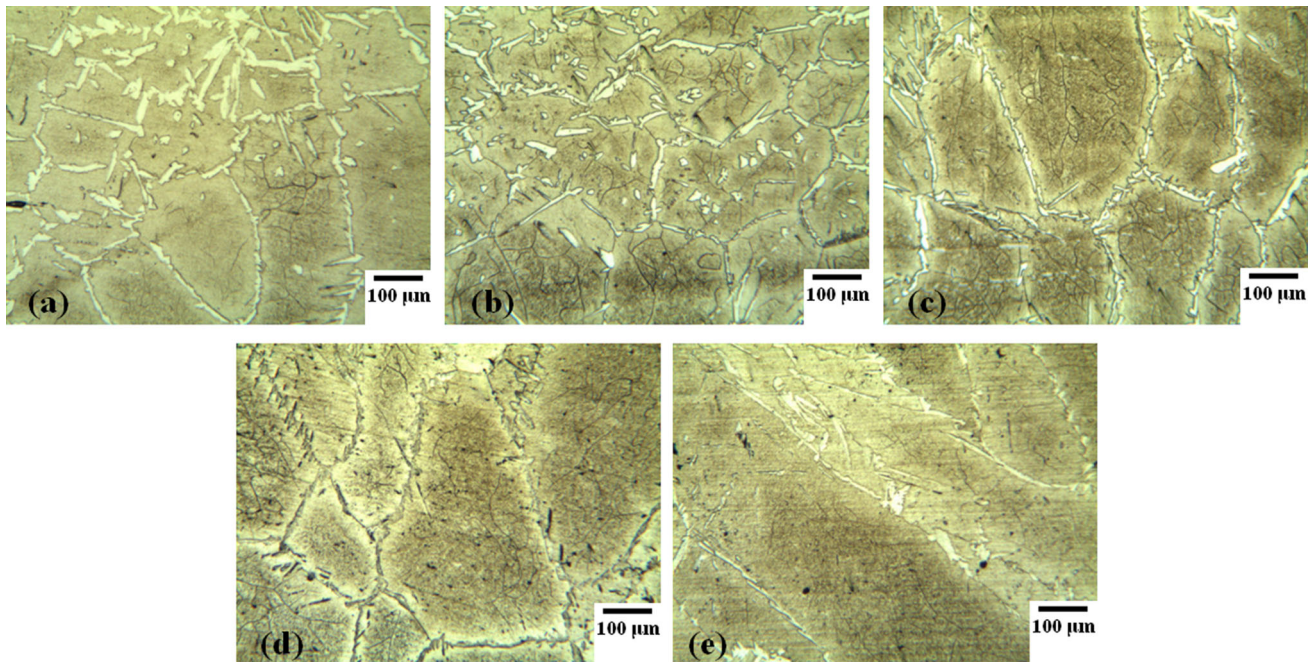


Fig. 4 The optical micrographs of the weld metal at different inter-pass temperatures (a) 750 °C (b) 550 °C (c) 350 °C (d) 150 °C and (e) 25 °C

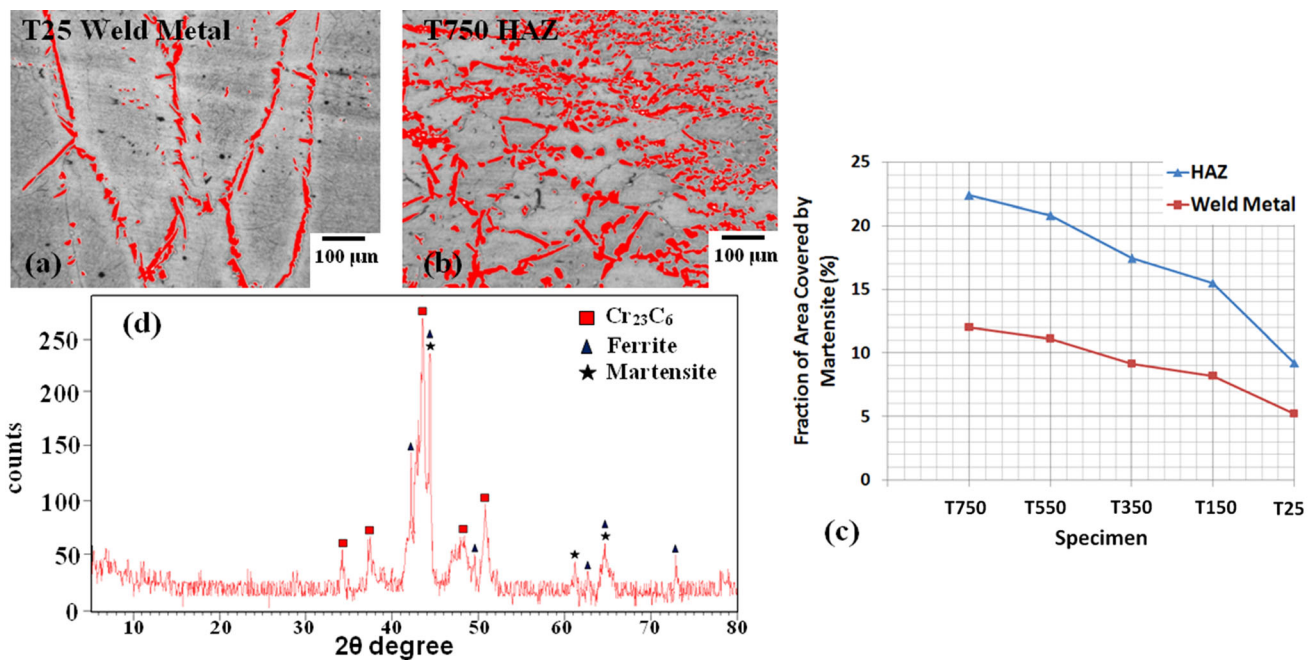


Fig. 5 The areas detected as martensite by Clemex software for (a) T25 weld metal and (b) T750 HAZ. (c) The fraction of area covered by martensite in the weld metal and the HAZ (d) the XRD graph of the weld metal confirming the presence of Cr₂₃C₆, martensite and ferrite

According to the weld metal composition in this study, k-factor reaches about 15 which is lower than the critical value of 17; therefore, martensite formation is predicted in the weld metals. It is noteworthy that XRD result in Fig. 5(d) signifies martensite phase in the weld metal which is consistent with microscopy images and also k-factor.

Mechanical properties of the welds are undoubtedly dependent upon several factors such as amount of martensite and the nature and degree of precipitations. So, a close investigation of

precipitated carbides can be helpful in analyzing mechanical properties of the specimens. According to the phase diagram in Fig. 1, the solubility of carbon drops dramatically upon cooling from 0.15 wt.% at 1400 °C to about 0.03 wt.% at 1000 °C; therefore, carbide precipitation is inevitable. At high cooling rates as in welding condition, significant intra-granular precipitation is observed. Figure 6(a) and (b) presents martensite plates and distribution of carbides in the weld metal of T750 specimen, respectively.

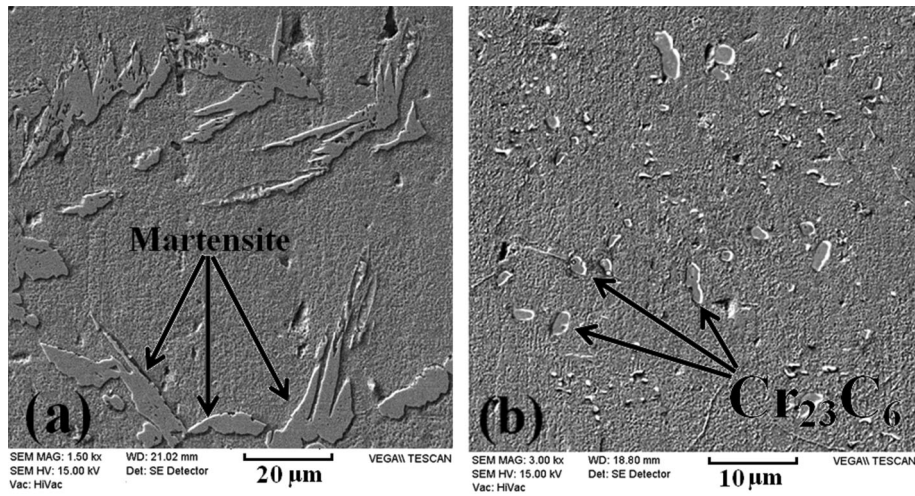


Fig. 6 SEM micrograph of the weld metal welded at an inter-pass temperature of 750 °C presenting (a) martensite plates (b) distribution of carbides

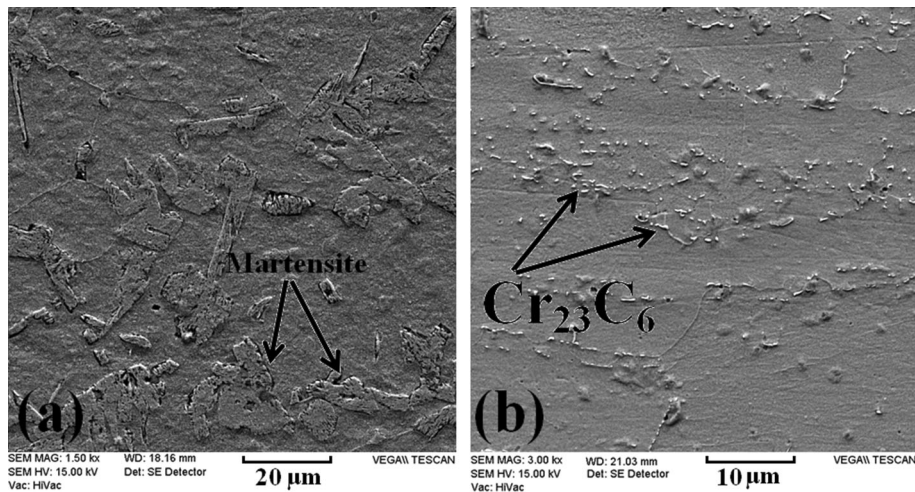


Fig. 7 SEM micrograph of the weld metal welded at an inter-pass temperature of 25 °C presenting (a) martensite plates (b) distribution of carbides

When cooling rate is high as in T25 specimen, there is not enough time for transformation of a large amount of ferrite to austenite on grain boundaries; hence, lower amount of martensite is formed (Fig. 7a). Moreover, by decreasing inter-pass temperature less carbide would have the chance to precipitate. According to Fig. 7(b), carbide formation is limited and small amount of tiny carbides precipitate in the ferrite matrix. At moderate cooling rate as in T150 specimen (Fig. 8a), larger lathy martensites in comparison with T25 specimen are present on the grain boundaries. According to Fig. 8(b), much more tiny carbides with a homogenously distributed pattern are seen in the ferritic matrix of T150 specimen.

According to Fig. 9(a), (b) and (c), one can see precipitate-free zone (PFZ) around martensite plates in the weld metal. Figure 9(a) is the optical micrograph of the weld metal for T750 specimen. As it is seen, thick martensite plates with wide PFZs are present in the microstructure. The dark peppery structure inside the grains shows the carbides that have formed during cooling. However, when cooling rate increases as in T150 weld metal in Fig. 9(b), martensite plates get thinner and

the width of PFZ remarkably decreases. PFZ in T25 weld metal with the highest cooling rate has been almost eliminated (Fig. 9c).

According to Fig. 10, different martensite patterns are obvious in the microstructure of the weld metal. Figure 10(a) shows the SEM micrograph of the weld metal in T750 specimen. The martensite in this case possesses a projected pattern (point A), while the martensite in the weld metal of T25 specimen in Fig. 10(b) has a dented pattern with adjacent parallel laths (point B). Distinct patterns relate to chemical compositions, especially carbon content of martensite (Ref 23).

3.3 Effect of Cooling Rate on Microstructure

In the present study, the cooling rate is predicted using Eq (2) (Ref 24).

$$R = 2\pi\lambda\rho C_P \left(\frac{t}{H}\right)^2 \times (T_C - T_0)^3 \quad (\text{Eq 2})$$

where (R) is the cooling rate (°C/s) at a point on the weld centerline at the moment when the metal passes through a

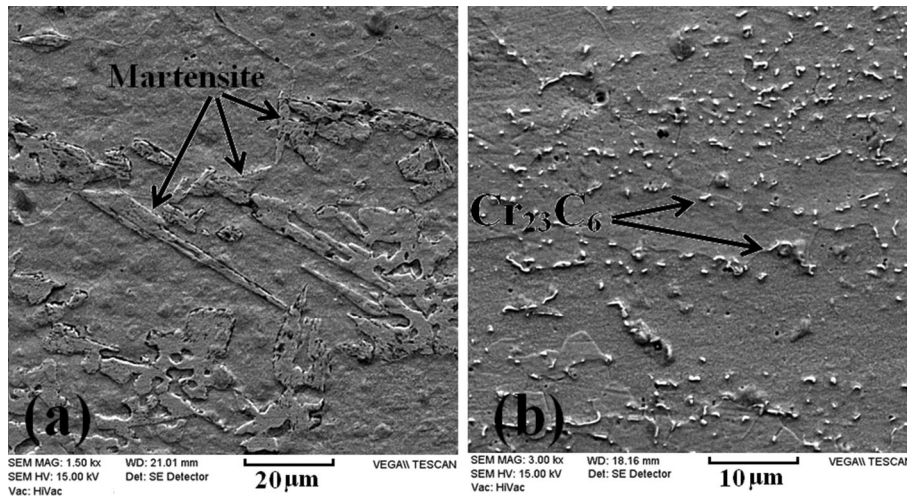


Fig. 8 SEM micrograph of the weld metal welded at an inter-pass temperature of 150 °C presenting (a) martensite plates (b) distribution of carbides

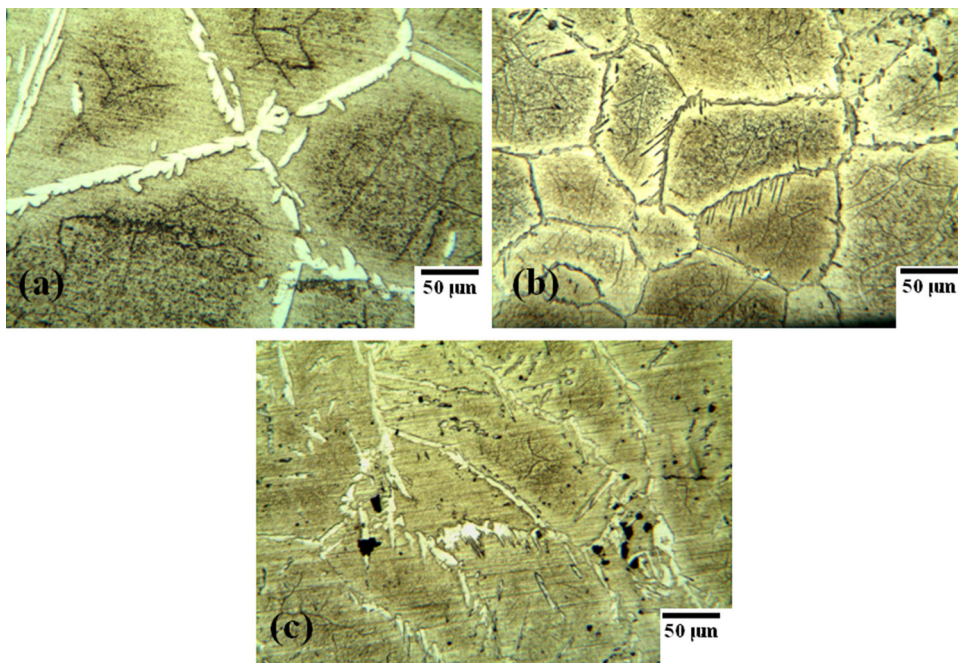


Fig. 9 The optical micrographs of precipitate-free zone (PFZ) around martensite plates in the weld metal at an inter-pass temperature of (a) 750 °C (b) 150 °C and (c) 25 °C

particular temperature of interest (T_c), (T_0) is the initial temperature (°C), (λ) is the thermal conductivity of the metal, (t) is the thickness of the base metal (mm), (H) is the net heat input used during welding, (ρ) is the density of the material (g/mm^3) and (C_p) is the specific heat of solid metal ($\text{J}/\text{g } ^\circ\text{C}$). These physical properties of the base metal are presented in Table 2. In the present study, the critical temperature (T_c) is supposed to be the temperature of δ -ferrite region start ($T_c = 1480$ °C) according to the phase diagram in Fig. 1. (T_0) is set as inter-pass temperature (750, 550, 350, 150 and 25 °C) for different specimens which were studied. Heat input is calculated as in Eq (3).

$$H = \eta \frac{E \cdot I}{v} \quad (\text{Eq } 3)$$

where (E) is the welding voltage (I), is the welding current (v) is the welding speed and (η) and is the heat transfer efficiency which is about 0.6 for TIG welding.

According to the continuous cooling transformation diagram adopted from Pisorius et al. (Ref 25) in Fig. 11(a) for the transformation of δ -ferrite to γ in HAZ of AISI 430 ferritic stainless steel, one can see that if the material temperature reaches about 1100 °C within about 2 s, i.e., with a cooling rate equal to 190(°C/s), no reversion to γ will occur and δ -ferrite will be maintained up to the room temperature. However, based on the estimated cooling rates in this study (7.45, 15.40, 27.62, 45.03 and 58.60 °C/s) for different specimens at different inter-pass temperatures (750, 550, 350, 150 and 25 °C), respectively, materials will contain significant fraction of elevated temper-

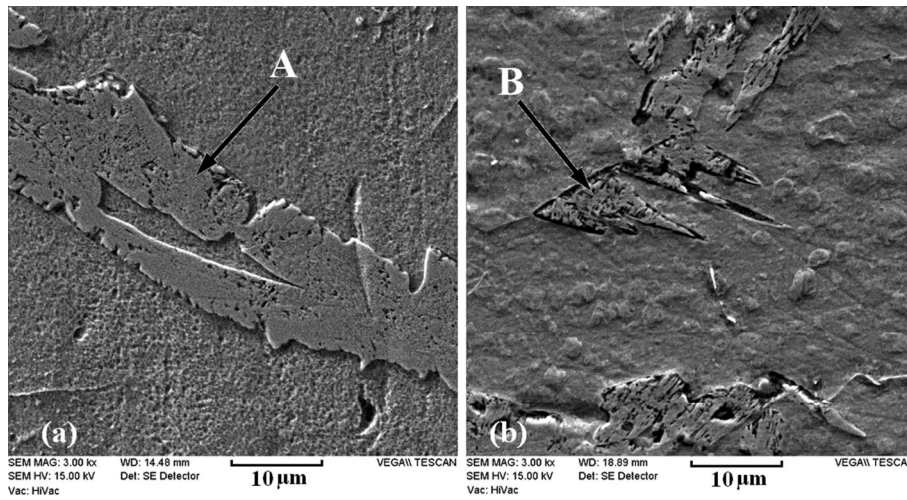


Fig. 10 SEM micrograph of different martensite patterns in the weld metal at an inter-pass temperature of (a) 750 °C (b) 25 °C

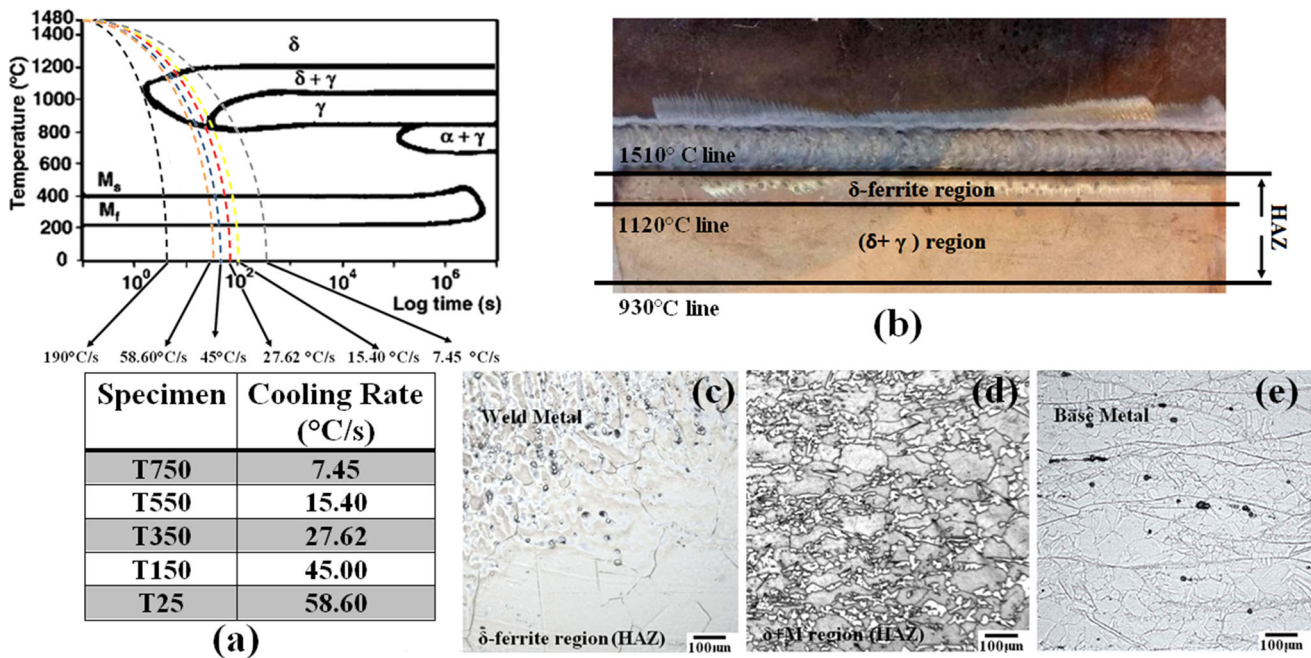


Fig. 11 (a) Continuous cooling transformation diagram for the transformation of δ -ferrite to γ in HAZ of AISI 430 ferritic stainless steel presenting different cooling rates at different inter-pass-temperatures (Ref 25) (b) top view of the weld metal presenting peak temperature boundaries and heat-affected zone. The optical micrograph presenting the sequence of microstructural variations from (c) near the fusion line (d) away from the fusion line in HAZ and (e) the base metal

ature austenite (γ) which will transform to martensite during cooling.

When inter-pass temperature decreases, cooling rate increases and the width of HAZ which includes δ -ferrite region and ($\delta + M$) region decreases. So, decreasing the width of fully δ -ferrite region can be obtained by controlling inter-pass temperature. By applying analytical equations for heat flow during welding, one can estimate the width of HAZ at different inter-pass temperatures. One of these equations was derived by Adams (Ref 26) for calculating the peak temperature at the workpiece surface at a distance (Y) away from the fusion line normal to the welding direction (Eq 4).

$$\frac{1}{T_p - T_0} = \frac{4.13vYt\rho C_p}{H} + \frac{1}{T_m - T_0} \quad (\text{Eq 4})$$

where (T_p) is peak temperature, (T_0) is workpiece temperature before welding (inter-pass temperature), (T_m) is melting temperature of the workpiece, (v) is travel speed, (t) is workpiece thickness, (H) is the heat transferred from the heat source to the workpiece, (ρ) is density and (C_p) is specific heat of the workpiece.

By applying temperatures at boundaries based on the phase diagram in Fig. 1 ($T_p = 1120$ and 930 °C), one can estimate the distance from the fusion line (Y) at which these peak

temperatures (T_p) are obtained at different inter-pass temperatures. Moreover, the difference between (Y) values at 1120 and 930 °C represents the estimated width of ($\delta + \gamma$) region. It should be noted that according to the phase diagram ($\delta + \gamma$) region is reached in an equilibrium condition; however, it is clear that during welding due to rapid cooling of the weld austenite (γ) will transform to martensite. Figure 11(b) represents the top view of the weld in which peak temperatures in HAZ have been schematically shown.

Table 4 shows the calculated data related to HAZ width based on applying different inter-pass temperatures. By increasing inter-pass temperature, the value of (Y), the width of δ -ferrite region and the width of ($\delta + \gamma$) region increase. According to this table, the width for δ -ferrite region increases dramatically from 0.72 to 4.12 mm by increasing the inter-pass temperature from 25 to 750 °C. Figure 11(c), (d) and (e) shows the sequence of microstructural variations from the weld metal to the base metal. Large δ -ferrite grains are detected near the fusion line in HAZ (Fig. 11c). These large grains would have detrimental effect on mechanical properties of the welds. Away from the fusion line in Fig. 11(d), smaller δ -ferrite grains with grain boundary martensite are visible. Martensite at grain boundaries prohibits from δ -ferrite grain coarsening.

3.4 Mechanical Properties of the Weldments

Figure 12 represents the hardness profile across the weld metal, HAZ and the base metal for the specimens. Two distinct regions are observed in HAZ. One region near the fusion line has the lowest microhardness that consists of coarse δ -ferrite grains, and the other region has high hardness values (~ 218 HV) containing duplex phases of δ -ferrite and martensite ($\delta + M$). By passing across the weld metal and entering HAZ, an abrupt drop in hardness is observed for all the specimens.

Figure 13 shows the stress–strain curves and the values of tensile strength of the welds. T750 specimen has the lowest tensile strength (367 MPa) and elongation (1.25%) compared to the other specimens due to large amount of martensite and blocky carbides in the weld metal. The highest tensile strength (487 Mpa) as well as highest elongation (23%) belongs to T150 specimen. According to this figure, it is seen that higher inter-pass temperatures than the optimum value of 150 °C result in lower tensile strength and ductility comparing with the condition when no inter-pass temperature is applied (T25 specimen). So, when it is not possible to have a precise control on inter-pass temperature during welding AISI 430 alloy, it is better to complete welding without inter-pass temperature to keep tensile strength and ductility of the weldments.

Figure 14(a) and (b) shows the fracture surface of T750 specimen. At low magnification in Fig. 14(a), a flat fracture

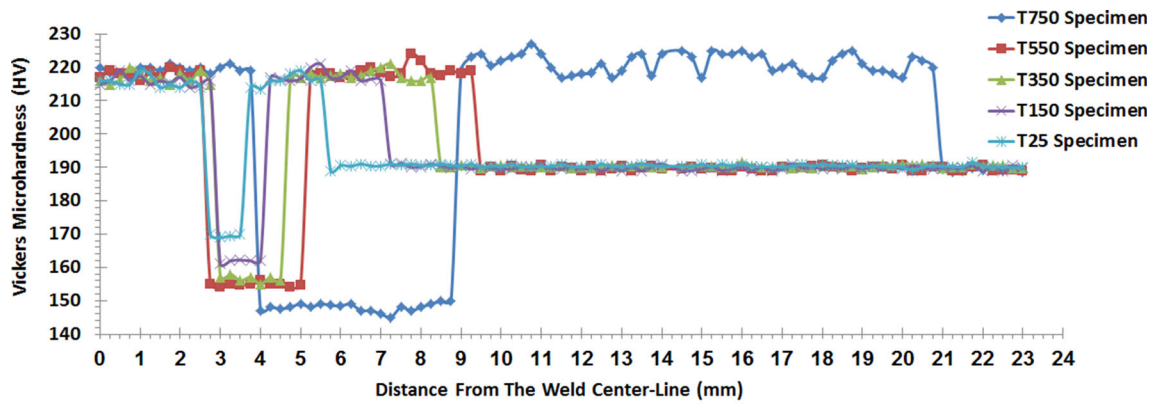
surface with many small facets is seen. The high magnification image in Fig. 14(b) shows that the dominant fracture behavior of T750 specimen is cleavage fracture indicating brittle failure. The fracture location of T750 specimen is shown in Fig. 14(c). As it is seen, the fracture takes place at approximately 5.5 mm away from the weld centerline. According to the hardness profile in Fig. 14 for T750 specimen, the failure is located in δ -ferrite region of HAZ (high-temperature heat-affected zone) where the lowest microhardness with coarse ferrite grains and carbide precipitates at ferrite grains is experienced. So, brittle fracture is expected. Figure 14(d) and (e) shows the fracture surface of T350 and T550 specimens, respectively. Both of the specimens show cleavage fracture indicating a brittle failure. The river pattern on cleavage facets which start from fine precipitates in the microstructure depicts the reduction in ductility and represents the brittle mode of fracture for the specimens. Figure 14(f) shows the location of fracture after tensile test for T350 specimen. As it is seen, the failure occurs approximately 4 mm away from the weld centerline where the lowest hardness distribution region was reported for this specimen as a result of excessive δ -ferrite grain coarsening.

Figure 15(a) (b), and (c) presents the fracture surface of T150 specimen. The scanning electron micrograph in Fig. 15(b) at low magnification reveals a quasi-cleavage rupture with two distinct regions (A and B) on the fracture surface indicating both ductile and brittle failure. The small facets in region (A) which are seen at higher magnification in Fig. 15(a) are resulted from cleavage and are surrounded by necklace-like bands. The bands consist of a collection of dimples. The dimples in region (B) are shown at high magnification in Fig. 15(c). The fracture location of T150 specimen is shown in Fig. 15(d). According to this figure, failure occurs at about 4.2 mm away from the weld centerline. Based on the microhardness profile in this region, the microstructure is somehow shifting from δ -ferrite with the lowest microhardness value to ($\delta + M$) with the highest microhardness value in HAZ. It means that the fracture site is δ -ferrite/($\delta + M$) interface which implies an important microstructure and local property change in this region.

Figure 16(b) shows the fracture surface of T25 specimen. A quasi-cleavage rupture with both ductile and brittle features is clearly seen on the fracture surface. Region (A) in Fig. 16(b) is shown at higher magnification in Fig. 16(a). Cleavage steps and tearing ridges with intergranular crack propagation in the fracture area confirms that the failure mode in this region is brittle fracture. Figure 16(c) which represents region (B) corresponding to Fig. 16(b) at higher magnification reveals that ductile regions are fractured by dimpled micro-void coalescence.

Table 4 The calculated data related to HAZ width based on applying different inter-pass temperatures

		“Y” (mm) value at different inter-pass temperatures				
		750 °C	550 °C	350 °C	150 °C	25 °C
Peak temperature (T_p) According to the phase diagram, °C	1120	4.12	2.12	1.30	0.88	0.72
	930	12.60	4.72	2.56	1.62	1.29
<i>Estimated HAZ width, mm</i>						
δ -ferrite region		4.12	2.12	1.30	0.88	0.72
($\delta + \gamma$) region		8.48	2.60	1.26	0.74	0.57



Average Microhardness (HV)

Specimen	Weld Metal	HAZ (δ)	HAZ ($\delta+M$)	Base Metal
T750	219.3±1.08	150±1.20	221.2±2.80	189.2±0.47
T550	218±1.28	154.8±0.55	218.7±1.76	189.6±0.55
T350	216.8±1.57	156.6±0.90	217.6±1.32	190.3±0.36
T150	216±1.27	161.8±0.43	217.4±1.60	189.9±0.57
T25	215.6±1.55	169.6±0.41	216±1.70	190.4±0.42

Fig. 12 The hardness profile across the weld metal, HAZ and the base metal for the specimens

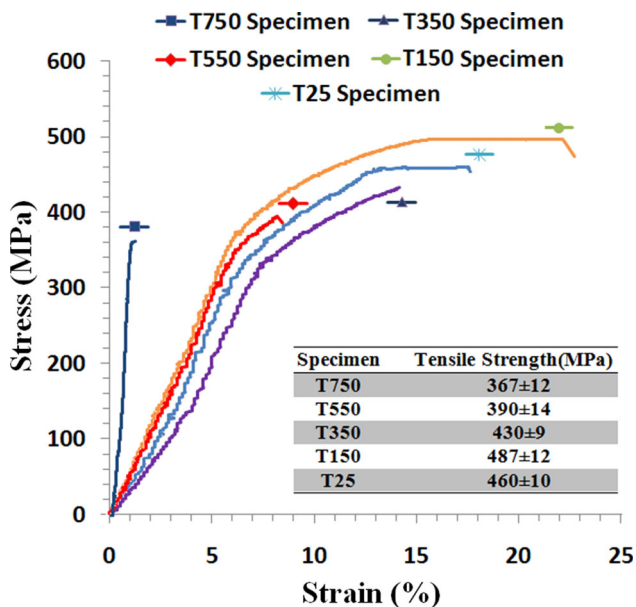


Fig. 13 The stress-strain curves and the values of tensile strength of the specimens at different inter-pass temperatures

4. Discussion

4.1 Microstructure in the Base Metal, HAZ and the Weld Metal

The dramatic grain growth especially near fusion line would have detrimental effects on mechanical properties of ferritic stainless steels. According to Fig. 2(c), at a lower inter-pass temperature, cooling rate increases and smaller δ -ferrite grains as well as thinner martensite plates at grain boundaries are observed. The average grain size in fully δ -ferrite region which obtained by mean intercept method for T25 specimen is about 75 μm , whereas the grain size for T750 specimen is more than

twice and is about 165 μm . Upon cooling, austenite transforms to martensite. So the microstructure in HAZ for all of the specimens consists of ferritic matrix with grain boundary martensite. As inter-pass temperature decreases, the amount of martensite at grain boundaries also decreases. T750 specimen experiences the highest inter-pass temperature (Fig. 3a). It means that cooling rate at HAZ is the lowest. By decreasing cooling rate, the sample remains for a longer period of time at ($\delta + \gamma$) region and more austenite forms at ferrite grain boundaries by solid-state phase transformation. By further cooling, more martensite plates form from austenite along the ferrite grain boundaries. On the other hand, as it is seen in T25 specimen in Fig. 3(e), when the second pass is laid on the first pass after a long period of time, i.e., applying no inter-pass temperature, HAZ would experience higher cooling rates. So, austenite has less time to form which in turn results in less amount of martensite by further cooling.

In the weld metal, at higher inter-pass temperatures, cooling rate decreases so the weld metal cools down slowly and the weld metal remains for longer period of times in ($\delta + \gamma$) region. So, austenite has the chance to form on δ -ferrite grain boundaries. By further cooling, the austenite transforms to martensite. As it is seen in Fig. 8, by increasing inter-pass temperature (T750), more martensite plates and also white carbide precipitates appear in the weld metal. Precipitation of carbide needs also the migration of carbon in ferrite matrix. So, when carbon atoms have sufficient time for carbide formation during cooling, the probability of precipitation of carbides increases and large blocky carbides are precipitated. The XRD pattern in Fig. 5(d) also confirms Cr_{23}C_6 precipitates in the weld metal of T750 specimen. These carbides form because of super-saturation of carbon in the ferrite at high temperature. These homogeneously distributed carbides would be undoubtedly effective on mechanical properties of the specimen.

Carbon atoms have higher solubility in elevated temperature austenite compared to ferrite; therefore, at high temperatures the austenite acts as sink for carbon and the local concentration of carbon in the ferrite reduces and there would be a little

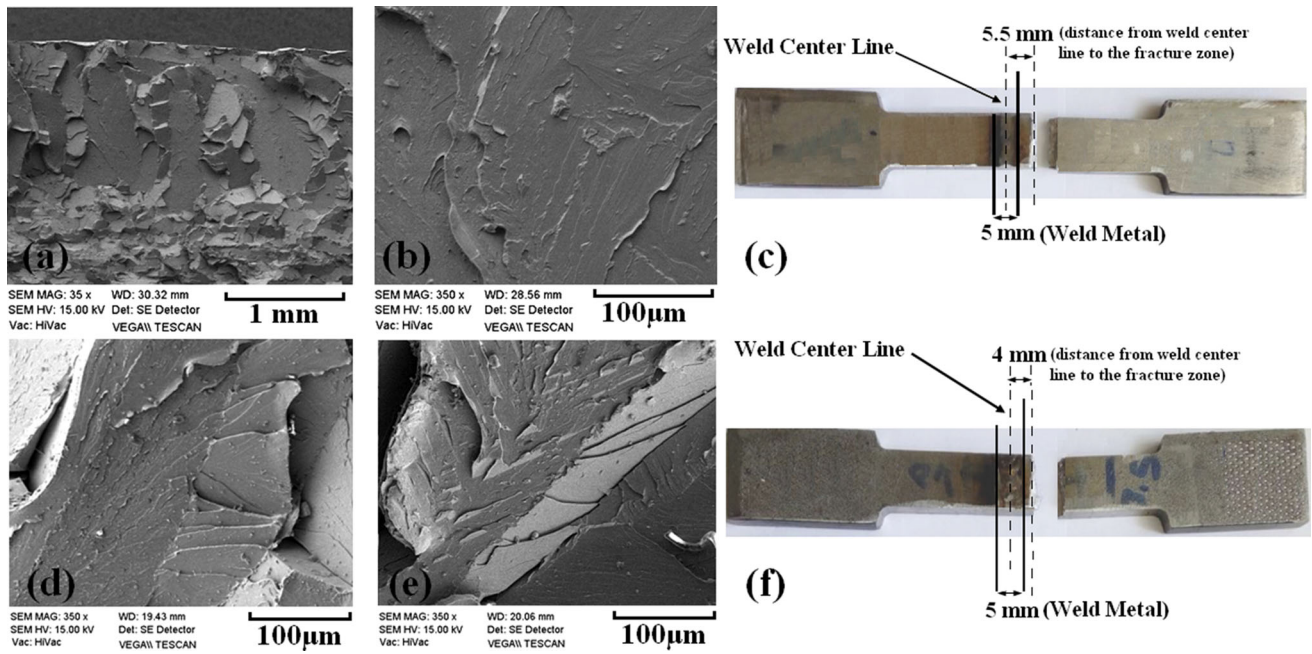


Fig. 14 The fracture surface of T750 specimen at (a) low magnification (b) high magnification (c) fracture location of T750 specimen and the fracture surface of (d) T350 and (e) T550 specimens indicating a brittle failure (f) fracture location of T350 specimen

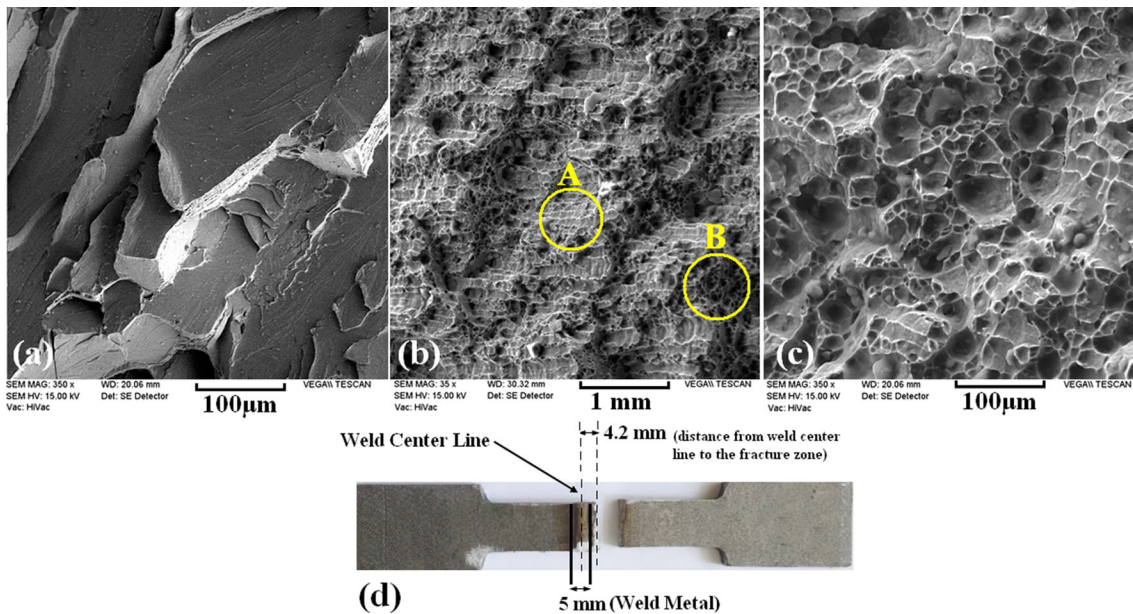


Fig. 15 The fracture surface of T150 specimen presenting (a) cleavage facets (b) quasi-cleavage fracture (c) ductile fracture by dimples (d) fracture location of T150 specimen

driving force for carbide precipitation (Ref 12). According to Fig. 9, the elevated temperature austenite transforms to martensite upon cooling and produces a narrow region free from carbon atoms. During cooling the weld metal to the temperature range of carbide precipitation, no carbide precipitates in this narrow region around the martensite plates. At lower cooling rates as in T750 weld metal, carbon atoms have enough time for short range diffusion from ferrite to elevated temperature austenite at grain boundaries; therefore, a wide region free from carbon atoms is formed which in turn results in a wide PFZ.

Upon cooling, the elevated temperature austenite transforms to thick martensite plates. On the other hand, because of higher cooling rate in T25 weld metal, carbon atoms do not have enough time to diffuse from longer distances to austenite phase and a narrow PFZ is formed. T750 specimen experiences a lower cooling rate. At elevated temperature, carbon tends to partition from the ferrite to the austenite due to higher solubility of carbon in austenite. This situation provides enough time for carbon migration. So, rich carbon austenite forms from ferrite matrix. Martensite with higher carbon content is expected when

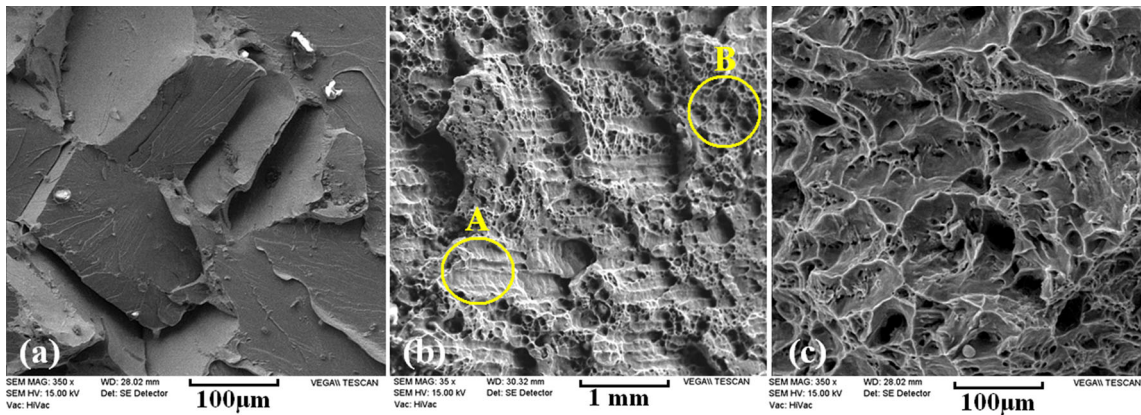


Fig. 16 The fracture surface of T25 specimen (a) cleavage facets with tearing ridges (b) quasi-cleavage fracture (c) ductile fracture by dimples

the carbon content of austenite is high. On the other hand, when cooling rate increases as in T25 specimen, martensite with lower carbon content is formed.

4.2 Mechanical Properties

The drop in hardness values in HAZ near the fusion line in comparison with the adjacent regions is due to δ -ferrite grain growth and also the absence of martensite at ferrite grain boundaries. It should be noted that the width of this low hardness region is different in the specimens. The width of HAZ in δ -ferrite region is larger for T750 specimen, so a longer distance of HAZ experiences low hardness values. On the other hand, the width of HAZ in δ -ferrite region for T25 specimen is not extended to far distances and a very short length of HAZ experiences low hardness values. The variation of hardness values in HAZ in δ -ferrite region for different specimens is due to different grain sizes as presented in Fig. 2(c) and (d). Larger δ -ferrite grains (165 μm) in T750 specimen lead to the least hardness values (~ 150 HV). After this sudden drop in hardness, the maximum hardness values (~ 218 HV) are obtained at the HAZ in ($\delta + M$) region. Formation of higher amount of martensite at ferrite grain boundaries at HAZ in ($\delta + M$) region increases the dislocation density which results in higher hardness in this region. Owing to higher inter-pass temperature, the length of HAZ in ($\delta + M$) region for T750 specimen is more than the other specimens. Such heterogeneous hardness profile in HAZ can be related to various phase transformations and heat cycles that occur in this region. By approaching the base metal, the hardness value decreases due to the lack of martensite. Hardness values show that the average hardness at the fusion zone of the weldments is found to be higher for all the weldments (~ 217 HV) compared to the base metal (~ 190 HV). This is due to the existence of large amount of martensite and finely dispersed carbides in the microstructure. The difference in martensite content of weld metal between T25 and T750 specimen is not very high and is less than 7%. This difference is also about 12% for low-temperature HAZ. It seems that such amount of martensite may not have a severe impact on hardness in weld metal or low-temperature HAZ. So, the variation of hardness values in the weld metal and low-temperature HAZ is not as much as high-temperature HAZ. It should be noted that lower amount of martensite in the weld metal comparing to low-temperature HAZ can be compensated by dispersed carbides in the weld metal.

The presence of hard untempered martensite with higher amount of carbon in comparison with other specimens would reduce the ductility of the weld and could act as stress raisers and crack initiation points (Ref 27). It is clear that controlling the amount of martensite is vital to improve the performance of ferritic stainless steel joints. T150 specimen has an optimized amount of low-carbon martensite and also finely dispersed carbides which can control the motion of dislocations and can contribute to the strength. When no inter-pass temperature is applied as in T25 specimen, the amount of martensite reduces significantly. High amount of martensite can be detrimental to tensile properties of AISI 430 stainless steel and low amount of martensite can also be harmful for the ductility of the weld. According to Mukherjee et al. (Ref 28), the grain growth of δ -ferrite at elevated temperatures can be limited by a fraction of martensite on the grain boundaries. Therefore, ductility would be improved in welds which contain some amount of martensite. On the other hand, less finely distributed carbide precipitates are seen in T25 weld metal in comparison with T150 specimen. So, tensile strength of T25 specimen drops to about 460 MPa. However, its strength is still higher than T750, T550 and T350 specimens. Therefore, it can be concluded that there is an optimum inter-pass temperature which results in the highest tensile strength and ductility. The failure location of the joints during the tensile test is consistent with hardness distribution profile. The failure occurred in all the joints along the lowest hardness distribution profile. Some of the specimens failed in the HAZ, near the fusion line at δ -ferrite region of the HAZ and some fractured at the interface of δ -ferrite and ($\delta + M$) region. T750, T550 and T350 specimens were fractured at δ -ferrite region of the HAZ where coarse δ -ferrite grains with the lowest microhardness are present. However, T150 and T25 specimens failed in the HAZ at the interface of δ -ferrite and ($\delta + M$) region. In fact, with an increase in tensile strength of the joints the fracture location changes from δ -ferrite region to interfaces in the HAZ where discontinuity in the microstructure is seen.

The presence of hard untempered martensite would reduce the ductility of the joints. However, one of the problems plaguing ferritic stainless steels is rapid grain growth at high temperature with subsequent brittleness. The presence of dimples in Fig. 15 means that some ductile fracture occurs in T150 specimen besides the dominant quasi-cleavage rupture which is coincident with the higher ductility of T150 specimen. The sharp transition of local mechanical properties results in

crack initiation in δ -ferrite at the interface with a cleavage fracture. According to (Ref 28), the dominant role in the toughness of the joints is played by grain size and the presence of martensite on ferrite grain boundaries. The grain growth of δ -ferrite at elevated temperature is limited by a fraction of martensite at grain boundaries and the cleavage is arrested at martensite colonies in ($\delta + M$) region of HAZ (Ref 29). Due to this effect, total energy absorbed during fracture will increase which in turn results in higher ductility of T150 specimen. The fracture site in T25 specimen is also at δ -ferrite/($\delta + M$) interface in HAZ as well as T150 specimen.

In a nutshell, this research addressed the autogenous welding of 430 alloy at different inter-pass temperatures. It is understood from the study that controlling inter-pass temperature is essential in welding AISI 430 alloy. Different inter-pass temperatures result in different martensite content and δ -ferrite grain size in the weld metal and in the HAZ. According to the relationship between microstructure and mechanical properties of the weldments, an optimum inter-pass temperature of 150 °C is recommended.

5. Conclusions

Autogenous TIG welding process was used to join AISI 430 ferritic stainless steels plates. The effect of inter-pass temperature was studied on the microstructure and mechanical properties of the weldments. The following are the main results drawn from the present study.

1. Increasing inter-pass temperature results in higher amount of grain boundary martensite in both weld metal and HAZ. Moreover, the HAZ width increases from about 1.3 mm to about 12 mm by increasing inter-pass temperature from 25 to 750 °C.
2. Two distinct regions in the HAZ of the specimens were detected. One region near the fusion line with the lowest microhardness that consists of coarse δ -ferrite grains and the other region with the highest hardness values containing duplex phases of δ -ferrite and martensite ($\delta + M$). This implies an important microstructure and local property change in this region with a sharp transition of local mechanical properties.
3. Applying high inter-pass temperatures such as 750 °C or 550 °C result in low tensile strength and ductility with completely brittle fracture surfaces, whereas the joints welded at 150 °C inter-pass temperature demonstrated the highest tensile strength and ductility.
4. When it is not possible to have a precise control on inter-pass temperature during manufacturing AISI 430 joints, it is better to complete welding without applying inter-pass temperature in order to at least keep tensile strength and ductility of the weldments.

Acknowledgments

The authors thank the support from Islamic Azad University for providing the funding for this research.

References

1. E. Folkhard, *Welding Metallurgy of Stainless Steel*, Springer, New York, 1984, p 172–178
2. N. Fujita, K. Ohmura, and A. Yamamoto, Changes of Microstructures and High Temperature Properties During High Temperature Service of Niobium Added Ferritic Stainless Steels, *Mater. Sci. Eng. A*, 2003, **351**, p 272–281
3. J. Honeycombe, Gooch TG Corrosion and Stress Corrosion of Arc Welds in 18% Chromium-2% Molybdenum-Titanium Stabilised Stainless Steel, *Br. Corros. J.*, 1983, **18**(1), p 25–34
4. L. Faivre, P.-O. Santacreu, and J. Leseux, Thermal Fatigue Resistance of Welded Joints in Stainless Steel High Temperature Exhaust Applications, *Technol. Metal. Mater.*, 2011, **8**(1), p 24–30
5. J.A. Sedricks, *Corrosion of Stainless Steels*, Wiley, Princeton, 1979, p 282
6. A.C.S. Sabioni, A.M. Huntz, E.C. Luz, M. Mantel, and C. Haut, Comparative Study of High Temperature Oxidation Behaviour in AISI, 304 and AISI, 439 Stainless Steels, *Mater. Res.*, 2003, **6**(2), p 179–185
7. F.B. Pickering, The Metallurgical Evolution of Stainless Steels, *Int. Met. Rev.*, 1976, **21**, p 227–278
8. J.C. Lippold and D.J. Kotecki, *Welding Metallurgy and Weldability of Stainless Steels*, Wiley, New York, 2005
9. M.B. Bilgin and C. Meran, The Effect of Tool Rotational and Traverse Speed on Friction Stir Weldability of AISI, 430 Ferritic Stainless Steels, *Mater. Des.*, 2012, **33**, p 376–383
10. G. Mallaiiah, A. Kumar, P.R. Reddy, and G.M. Reddy, Influence of Grain Refining Elements on Mechanical Properties of AISI, 430 Ferritic Stainless Steel Weldments—Taguchi Approach, *Mater. Des.*, 2012, **36**, p 443–450
11. V. Anbazhagan and R. Nagalakshmi, Metallurgical Studies in Ferritic Stainless Steel, *Weld. Res. J.*, 2002, **23**, p 25–37
12. M. Alizadeh-Sh, S.P.H. Marashi, and M. Pouranvari, Resistance Spot Welding of AISI, 430 Ferritic Stainless Steel: Phase Transformations and Mechanical Properties, *Mater. Des.*, 2014, **56**, p 258–263
13. D.K. Ramkumar, A. Chandrasekhar, A. Kumar Singh, S. Ahuja, A. Agarwal, N. Arivazhagan, and A. Maximus Rabel, Comparative Studies on the Weldability, Microstructure and Tensile Properties of Autogeneous TIG Welded AISI, 430 Ferritic Stainless Steel with and Without Flux, *J. Manuf. Process.*, 2015, **20**, p 54–69
14. C.C. Hsieh, D.Y. Lin, M.C. Che, and W. Wu, Precipitation and Strengthening Behavior of Massive δ -Ferrite in Dissimilar Stainless Steels During Massive Phase Transformation, *Mater. Sci. Eng. A*, 2008, **477**, p 328–333
15. S. Ghorbani, R. Ghasemi, R. Ebrahimi-Kahrizsangi, and A. Hojjati-Najafabadi, Effect of Post Weld Heat Treatment (PWHT) on the Microstructure, Mechanical Properties, and Corrosion Resistance of Dissimilar Stainless Steels, *Mater. Sci. Eng. A*, 2017, **688**, p 470–479
16. S. Kou, *Welding Metallurgy*, 2nd ed., Wiley, New York, 2003, p 55–57
17. B.J. Ginn, T.G. Gooch, and T.G. Davey, Effects of Interpass Temperature When Welding Austenitic Stainless Steel, *Met. Constr.*, 1983, **15**(12), p 745–752
18. A.A. Omar, Effects of Welding Parameters on Hard Zone Formation at Dissimilar Welds, *Weld. J.*, 1998, **67**, p 86–93
19. C.H. Lee, *The Effect of Preheat and Interpass Temperature on Corrosion Behavior of Austenitic Stainless Steel*, AWS Convention, Dallas, 1984, p 197–199
20. S. Sam, C.R. Das, V. Ramasubbu, S.K. Albert, A.K. Bhaduri, T. Jayakumar, and E. Rajendra Kumar, Delta Ferrite in the Weld Metal of Reduced Activation Ferritic Martensitic Steel, *J. Nucl. Mater.*, 2014, **455**, p 343–348
21. J. Verma, R.V. Taiwade, R. Kataria, and A. Kumar, Welding and Electrochemical Behavior of Ferritic AISI, 430 and Austeno-Ferritic UNS 32205 Dissimilar Welds, *J. Manuf. Process.*, 2018, **34**, p 292–302
22. R.H. Kaltenhauser, Improving the Engineering Properties of Ferritic Stainless Steels, *Met. Eng. Q.*, 1971, **11**(2), p 41–47
23. M. Sarkari Khorrami, M.A. Mostafaei, H. Pouraliakbar, and A.H. Kokabi, Study on Microstructure and Mechanical Characteristics of Low-Carbon Steel and Ferritic Stainless Steel Joints, *Mater. Sci. Eng. A*, 2014, **608**, p 35–45
24. ASM Handbook, *Welding, Brazing and Soldering*, 10th ed., ASM International, Cleveland, 1993

25. P.G.H. Pistorius and G.T. van Rooyen, Composition and Properties of Ferritic Stainless Steels with Good Weldability, *Weld. World*, 1995, **36**(6), p 65–72
26. C.M. Adams, Cooling Rates and Peak Temperatures in Fusion Welding, *Weld. J.*, 1958, **37**, p 210–215
27. R.G. Cambell, Ferritic Stainless Steel Welding Metallurgy, *Eng. Mater.*, 1992, **69**, p 167–216
28. M. Mukherjee, A. Dutta, P. Kanjilal, T.K. Pal, and S. Sisodia, Enhancement of Microstructural and Mechanical Properties by Pulse Mode of Metal Transfer in Welded Modified Ferritic Stainless Steel, *ISIJ Int.*, 2015, **55**(7), p 1439–1447
29. T.G. Gooch and B.J. Ginn, *Report from the Cooperative Research Program for Research Members Only*, The Welding Institute, Cambridge, 1988, p 3–306

Publisher's Note Springer Nature remains neutral with regard to jurisdictional claims in published maps and institutional affiliations.